ChemPhysMater 3 (2024) 111–117

Contents lists available at ScienceDirect

ChemPhysMater

journal homepage: https://www.keaipublishing.com/en/journals/chemphysmater/

Research Article

High-entropy oxide, $(FeCoNiMnV)_xO$, boost the oxygen evolution

Chendong Kou[a], Meiling Qin[b], Wei Song[b], Weijun Zhu[b], Jieshu Zhou[a], Christopher Dorma Momo Jr[a], Hongyan Liang[a,*]

[a] School of Materials Science and Engineering, Tianjin University, Tianjin 300350, China
[b] CETC Deqing Huaying Electronics Co., Ltd., China

ARTICLE INFO

Keywords:
High-entropy oxides
Solvothermal method
Oxygen evolution reaction
Water splitting

ABSTRACT

The sluggish kinetics of the oxygen evolution reaction (OER), an essential half-reaction of water splitting, lead to high OER overpotential and low energy-conversion efficiency, hampering its industrial application. Therefore, considerable attention has been paid to the development of efficient catalysts to accelerate the OER. In this study, we synthesized the high-entropy oxides $[(FeCoNiMnV)_xO]$ and used them as efficient OER catalysts. A simple oil-phase method was used to synthesize $(FeCoNiMnV)_xO$. The catalytic performances of the $(FeCoNiMnV)_xO$ catalysts were modified by tuning the reaction temperature. The optimized $(FeCoNiMnV)_xO$ catalyst exhibited multiple elemental interactions and abundant exposed active sites, leading to an overpotential of approximately 264 mV to reach a current density of 10 mA cm^{-2} in 1 M KOH and stability of 50 h at 1000 mA cm^{-2}. Thus, a highly active OER catalyst was synthesized. This study provides an efficient approach for the synthesis of high-entropy oxides.

1. Introduction

Hydrogen, a clean and sustainable energy carrier for storing intermittent solar, wind, or tidal energy, can be produced using electrochemical water-splitting technology [1–5]. However, the sluggish kinetics of the oxygen evolution reaction (OER) results in high overpotential, hampering efficient energy conversion [6–10]. Owing to their intrinsic electrochemical characteristics, platinum-group metals (such as Ru and Ir) are employed to synthesize commercial OER catalysts [11–14]. However, the high cost and scarcity of platinum-group metals impede the widespread industrial application of the OER catalysts [15–18]. There has been growing interest in developing efficient OER catalysts using earth-abundant non-platinum group metals or metal compounds [19–21].

Transition metal oxides have been considered alternative candidates for synthesizing the OER catalysts because of their low cost and good catalytic performance [22,23]. Furthermore, multi-metal oxides exhibit superior catalytic activity compared with single-metal oxides, attributed to the synergistic interactions between multiple catalytically active sites [24]. For example, Wei et al. found that the OER activity of Co_3O_4 was significantly enhanced by introducing high-valent vanadium ions [25]. In addition, Zhang et al. demonstrated that $(Co_{0.2}Mn_{0.2}Ni_{0.2}Fe_{0.2}Zn_{0.2})Fe_2O_4$ had a single-phase structure and exhibited more efficient OER activity [26]. Consequently, multiple transition metal oxides incorporating multiple catalytically active sites are significant for designing the OER catalysts. Therefore, high-entropy oxides comprising five or approximately equimolar metals in a single-phase lattice with a random distribution [27] are considered promising OER catalysts.

In this study, we synthesized the high-entropy oxides $[(FeCoNiMnV)_xO]$ using a simple solvothermal method. Oleylamine was used as the solvent, glucose was used as the reducing agent, and different metallic salts were used as precursors. The reaction was carried out at different temperatures to obtain $(FeCoNiMnV)_xO$ catalysts with different properties. The $(FeCoNiMnV)_xO$ catalyst obtained at 220 °C had the highest active region. The $(FeCoNiMnV)_xO$ catalyst exhibited an overpotential of approximately 264 mV to reach a current density of 10 mA cm^{-2} in 1 M KOH and stability of 50 h at 1000 mA cm^{-2} owing to the high-entropy effects and abundant exposed active sites.

2. Experimental section

2.1. Chemicals

Cobalt acetylacetonate ($Co(acac)_2$, 97%), iron acetylacetonate ($Fe(acac)_3$, 97%), Nafion (5 wt%), and N-hexadecyltrimethylammonium chloride (CTAC, 96%) were purchased from Shanghai Aladdin Reagent Co., Ltd. Nickel acetylacetonate hydrate ($Ni(acac)_2$, 95%) was purchased from Shanghai Meryer Chemical Technology

---

* Corresponding author.
E-mail address: hongyan.liang@tju.edu.cn (H. Liang).

https://doi.org/10.1016/j.chphma.2023.08.002
Received 15 June 2023; Received in revised form 5 August 2023; Accepted 24 August 2023

Co., Ltd. Manganese acetylacetonate (Mn(acac)$_3$, 97%), vanadium oxy(acetylacetonate) (VO(acac)$_2$, 95%), glucose, molybdenum hexacarbonyl (Mo(CO)$_6$, 98%), and oleylamine (OAm, > 70%) were purchased from Tianjin Xiensi Biochemical Technology Co., Ltd. KOH (95%) was purchased from Shanghai Macklin Biochemical Co., Ltd. All chemicals were used without further purification. The deionized water obtained from the Milli-Q ultrapure water system was used in all experiments.

2.2. Synthesis of catalysts

(FeCoNiMnV)$_x$O was prepared using a low-temperature oil-phase method. Oleylamine (100 mL) was placed in a 250 mL vial, and CTAC (1000 mg) was added. The resulting mixture was sonicated for 25 min. Subsequently, Ni(acac)$_2$ (6.4 mg), Co(acac)$_3$ (8.9 mg), Fe(acac)$_3$ (8.8 mg), V(acac)$_2$ (6.5 mg), Mn(acac)$_2$ (6.5 mg), Mo(CO)$_6$ (33 mg), and glucose (60 mg) were added to the vial. The mixture

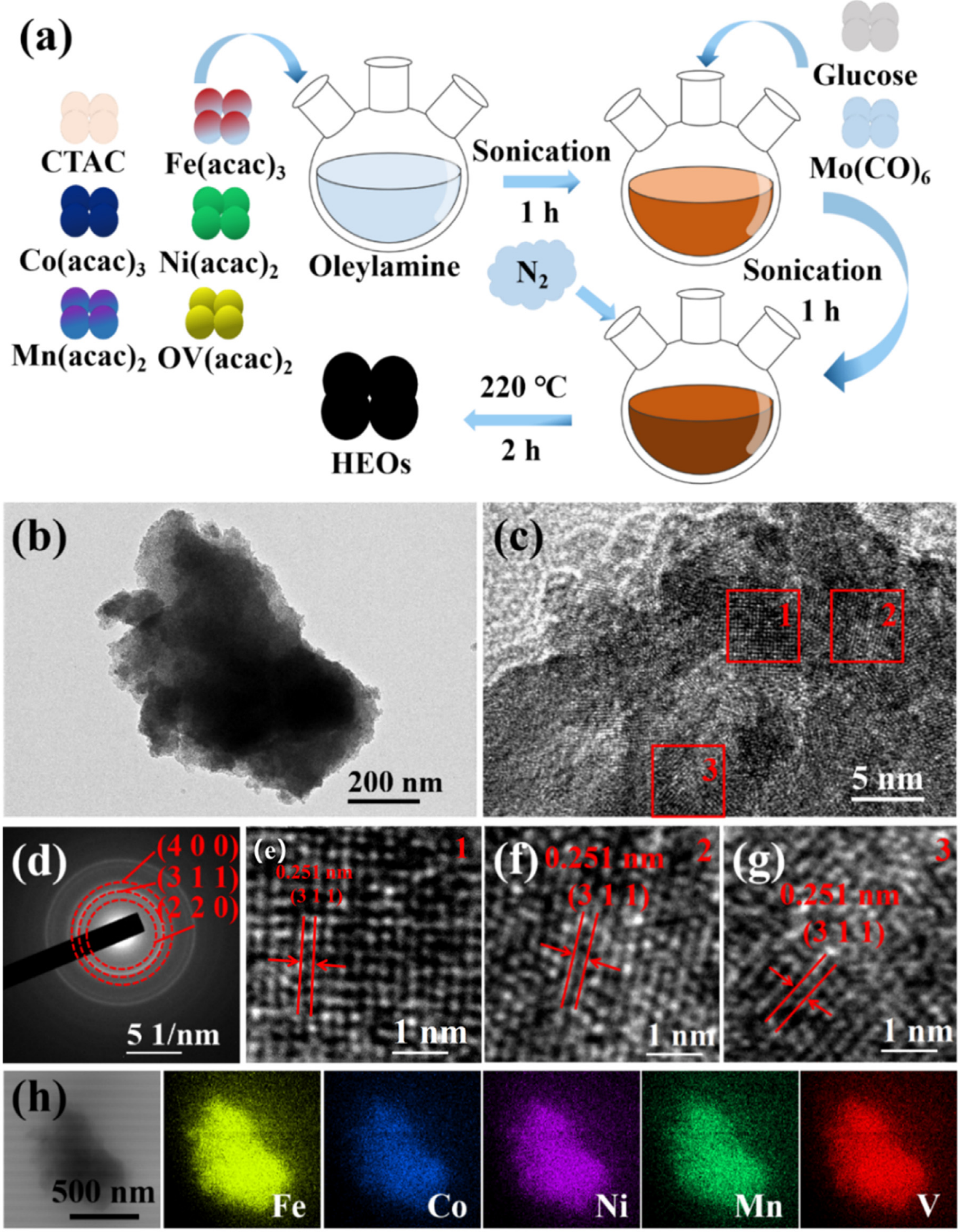

Fig. 1. (a) Schematics for the preparation of the (FeCoNiMnV)$_x$O catalyst, (b) TEM image, (c) HRTEM image, and (d) SAED pattern of the (FeCoNiMnV)$_x$O catalyst, (e)–(g) enlarged images for the three regions marked in (c), and (h) elemental mapping images of the (FeCoNiMnV)$_x$O catalyst obtained via TEM-EDS analysis.

was sonicated for 1 h to obtain a homogeneous solution. The solution was gradually heated to 220 °C at a rate of 5 °C min^{-1} and kept under magnetic stirring at 300 r/min for 2 h. The solution was centrifuged, and the black colloidal particles were collected. The particles were washed five times using an ethanol/cyclohexane mixture. The obtained material was dried in an oven at 60 °C for 24 h. Subsequently, the material was ground for further use. A similar methodology was used to synthesize $(FeCoNiMnV)_xO$-200 and $(FeCoNiMnV)_xO$-240 at a reaction temperature of 200 and 240 °C, respectively.

For the working electrode, we prepared a dispersion by mixing 5 mg of $(FeCoNiMnV)_xO$ powder with a mixed solution of 500 µL water, 480 µL isopropanol, and 20 µL Nafion. The resulting suspension was subjected to continuous sonication for a minimum of 1 h. Subsequently, the catalyst ink was deposited on a nickel foam (NF) substrate with an exposed working area of 0.5 cm^{-1} × 0.5 cm^{-1}. The coated substrate was allowed to dry overnight at room temperature, resulting in a catalyst loading of approximately 20 mg cm^{-2}.

2.3. Material characterizations

The morphologies of the prepared catalysts were examined using transmission electron microscopy (TEM, JEM-2100F), and energy-dispersive X-ray spectroscopy (EDS) was used to analyze the elemental distribution. The phase composition and crystallinity of the catalysts were characterized by powder X-ray diffraction (XRD, Bruker D8) using Cu Kα radiation. X-ray photoelectron spectroscopy (XPS, Thermo ESCALAB 250XI) was used to investigate the chemical states of the elements on the surface of the catalysts.

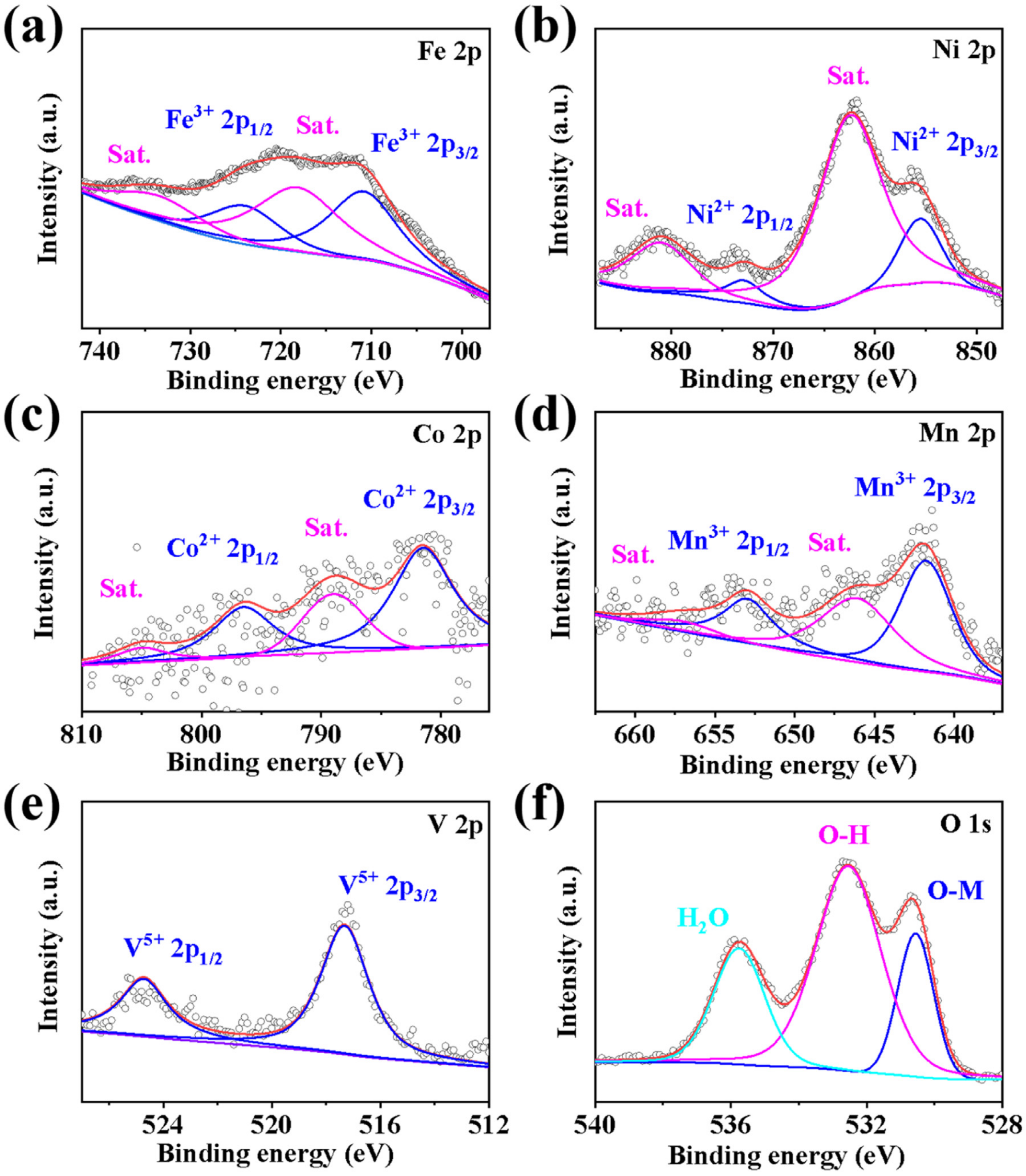

Fig. 2. XPS spectra of (a) Fe 2p, (b) Ni 2p, (c) Co 2p, (d) Mn 2p, (e) V 2p, and (f) O 1s of the $(FeCoNiMnV)_xO$ catalyst.

2.4. Electrochemical measurements

Electrochemical characterization of the catalysts was conducted using a CHENHUA electrochemical workstation and an Autolab PGSTAT 302 N electrochemical analyzer with a typical three-electrode system in 1 M KOH. The NF coated with catalyst (0.5 cm × 0.5 cm) was used as the working electrode, Ag/AgCl (saturated KCl) as the reference electrode, and Pt foil as the counter electrode. All potential measurements (vs. Ag/AgCl) were converted to the reversible hydrogen electrode (RHE) reference scale based on the Nernst equation ($E_{\mathrm{RHE}} = E_{\mathrm{measured}} + E^0{}_{\mathrm{Ag/AgCl}} + 0.0591 \times \mathrm{pH}$, $E^0{}_{\mathrm{Ag/AgCl}} = 0.197$ V at 25 °C and pH = 14). The catalyst was activated through 20 cycles of cyclic voltammetry (CV) scans ranging from 0 to 0.8 V (vs. Ag/AgCl) at a scan rate of 50 mV s^{-1}. Subsequently, linear sweep voltammetry (LSV) was carried out in the same voltage range but at a lower scan rate of 1 mV s^{-1}.

The Tafel slope, a parameter that characterizes the reaction kinetics of catalysts, was determined by analyzing the linear region of the LSV polarization curve. The Tafel equation, $\eta = a \times \log j + b$, where η represents the overpotential, a denotes the Tafel slope, and j represents the current density, was used for this analysis. Electrochemical impedance spectroscopy (EIS) was used to investigate the reaction kinetics of the catalysts. EIS measurements were conducted in a frequency range from 0.01 Hz to 100 kHz, with an amplitude of 5 mV and an overpotential of 300 mV [28]. The electrochemically active surface area (ECSA) and double-layer capacitance (C_{dl}) were obtained by analyzing the CV scans in the non-Faradaic region at scan rates ranging from 10 to 100 mV s^{-1} [29,30]. Chronopotentiometric measurements were performed at a fixed current density of 1000 mA cm^{-2} to assess the stability of the catalyst. During the electrochemical data analysis, an 85% *iR* correction was applied without additional notes. Here, "*R*" represents the solution resistance (R_s) mentioned in the impedance data.

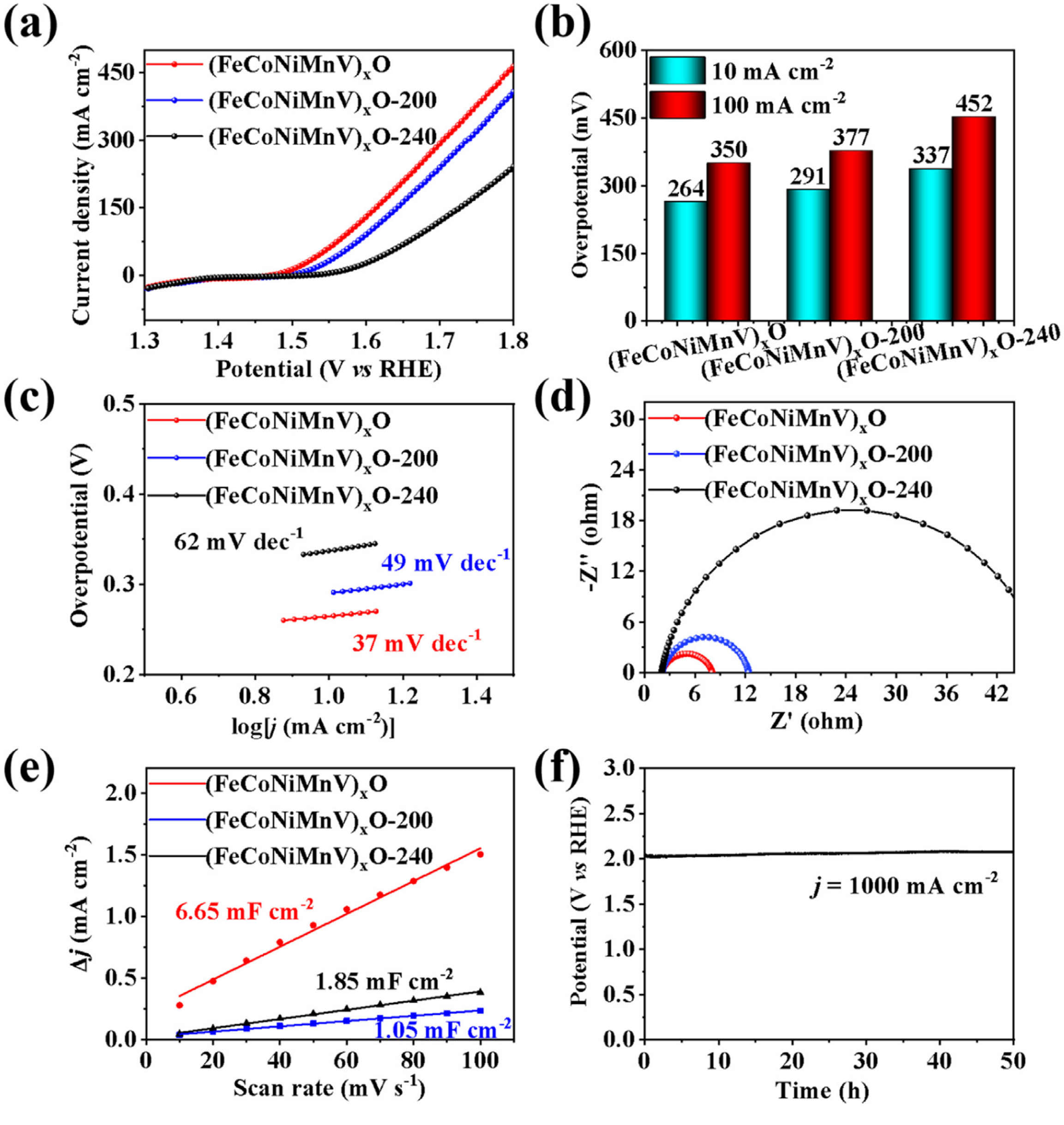

Fig. 3. Characterizations for assessing the catalytic performance of the OER. (a) LSV curves, (b) overpotential at the current density of 10 and 100 mA cm^{-2}, (c) Tafel plots, (d) Nyquist plots, and (e) linear fitting of C_{dl} of $(\mathrm{FeCoNiMnV})_x\mathrm{O}$, $(\mathrm{FeCoNiMnV})_x\mathrm{O}$-200, and $(\mathrm{FeCoNiMnV})_x\mathrm{O}$-240 catalysts in 1 M KOH, (f) chronopotentiometric curve at a current density of 1000 mA cm^{-2} in 1 M KOH without *iR* correction.

3. Results and discussion

3.1. Characterization of synthesized pre-catalysts

$(FeCoNiMnV)_xO$ catalysts were synthesized via a low-temperature oil-phase method, as shown in Fig. 1(a). Oleylamine was used as the solvent, glucose was used as the reducing agent, and different metallic salts were used as precursors. The black colloidal particles were collected after heating at 200, 220, or 240 °C for 2 h under magnetic stirring. The morphology, crystal structure, and elemental distribution of the $(FeCoNiMnV)_xO$ catalyst were analyzed. The XRD pattern of the $(FeCoNiMnV)_xO$ catalyst is presented in Fig. S1. The peaks at 30.3°, 35.7°, 43.4°, 57.4°, and 63.0° correspond to the (2 2 0), (3 1 1), (4 0 0), (5 1 1), and (4 4 0) planes of $NiFe_2O_4$ (PDF#74–2081), respectively [31,32]. TEM and high-resolution TEM (HRTEM) images of the $(FeCoNiMnV)_xO$ catalyst are shown in Figs. 1(b)(c), respectively. The interplanar distances are 0.251 and 0.286 nm, corresponding to the (3 1 1) and (4 0 0) planes of the $NiFe_2O_4$ phase, respectively (Figs. 1(e)–(g)) [31]. Furthermore, the selected area electron diffraction (SAED) pattern of the $(FeCoNiMnV)_xO$ catalyst (Fig. 1(d)) fits well with the (4 0 0), (3 1 1), and (2 2 0) planes of $NiFe_2O_4$. Moreover, the TEM-EDS elemental mapping images (Fig. 1(h)) and EDS spectra (Fig. S2) of the $(FeCoNiMnV)_xO$ catalyst confirmed the uniform dispersion of Fe, Ni, Co, Mn, and V.

XPS was conducted to analyze the valence states of the elements in the $(FeCoNiMnV)_xO$ catalyst. The high-resolution XPS spectra obtained are shown in Fig. 2. The Fe 2p spectrum (Fig. 2(a)) reveals two prominent peaks at 710.8 and 723.9 eV, corresponding to Fe^{3+} $2p_{3/2}$ and Fe^{3+} $2p_{1/2}$, respectively [33,34]. The Ni 2p spectrum (Fig. 2(b)) displays two prominent peaks at 855.6 and 872.9 eV, assigned to Ni^{2+} $2p_{3/2}$ and Ni^{2+} $2p_{1/2}$, respectively [9,25,35]. The Co 2p spectrum (Fig. 2(c)) exhibits two peaks at 781.5 and 796.5 eV, assigned to Co^{2+} $2p_{3/2}$ and Co^{2+} $2p_{1/2}$, respectively [36,37]. The Mn 2p spectrum (Fig. 2(d)) exhibits two characteristic peaks at 641.8 and 653.0 eV, corresponding to Mn^{3+} $2p_{3/2}$ and Mn^{3+} $2p_{1/2}$, respectively [38,39]. The V 2p spectrum (Fig. 2(e)) displays two peaks at 517.3 and 524.7 eV, representing V^{5+} $2p_{3/2}$ and V^{5+} $2p_{1/2}$, respectively [40,41]. The O 1s spectrum (Fig. 2(f)) exhibits three peaks at 530.5, 532.5, and 535.7 eV, assigned to O–M, O–H, and adsorbed water (H_2O), respectively [42]. The XPS results provide insights into the valence states of the elements in the $(FeCoNiMnV)_xO$ catalyst. In addition, we re-recorded the XPS spectra of the catalysts after 20 CV cycles (Fig. S3). The valence states of the metals did not change significantly, indicating the good stability of the $(FeCoNiMnV)_xO$ catalyst.

3.2. Electrocatalytic performance for OER

The electrocatalytic performance of the $(FeCoNiMnV)_xO$ catalyst for the OER was assessed using a conventional three-electrode system in an alkaline environment (1 M KOH). Before the electrocatalytic evaluation, the catalyst underwent 20 CV cycles for electrochemical pre-activation. The $(FeCoNiMnV)_xO$-200 and $(FeCoNiMnV)_xO$-240 catalysts were compared under identical experimental conditions.

Among the three $(FeCoNiMnV)_xO$ catalysts synthesized at different reaction temperatures, the $(FeCoNiMnV)_xO$-220 catalyst exhibits the lowest overpotential (approximately 264 mV) to achieve a current density of 10 mA cm^{-2} (Fig. 3(a)). The overpotentials of the $(FeCoNiMnV)_xO$, $(FeCoNiMnV)_xO$-200, and $(FeCoNiMnV)_xO$-240 catalysts at the current density of 10 and 100 mA cm^{-2} are illustrated in Fig. 3(b). The OER activity of the catalysts synthesized in this study was compared with those of other reported OER catalysts, as shown in Table S1, confirming the remarkable OER activity of the $(FeCoNiMnV)_xO$ catalysts. The corresponding Tafel plots were tested (Fig. 3(c)), where a smaller Tafel slope indicates a faster reaction rate, explaining the OER kinetics. The Tafel slopes

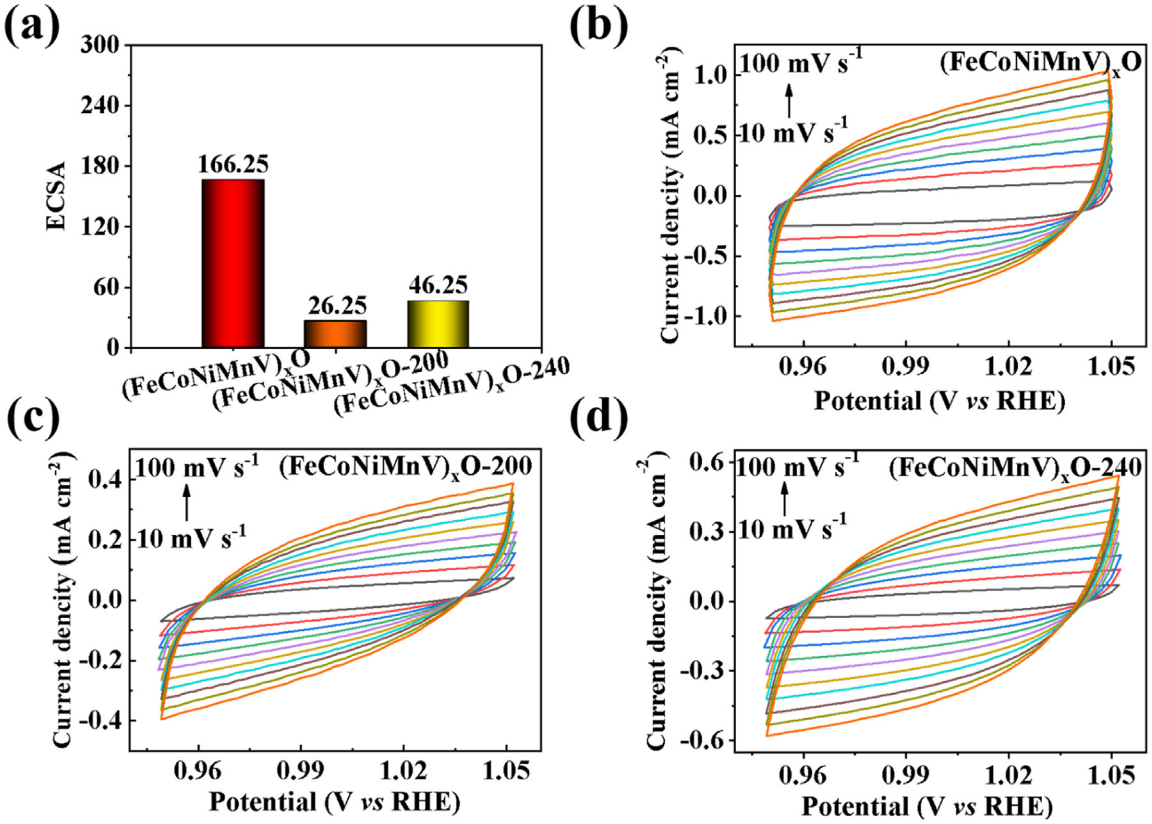

Fig. 4. (a) ECSA value and CV curves of the (b) $(FeCoNiMnV)_xO$, (c) $(FeCoNiMnV)_xO$-200, and (d) $(FeCoNiMnV)_x$-240 catalysts at scan rates of 10, 20, 30, 40, 50, 60, 70, 80, 90, and 100 mV s^{-1} in the non-faradaic region.

for the $(FeCoNiMnV)_xO$, $(FeCoNiMnV)_xO$-200, and $(FeCoNiMnV)_xO$-240 catalysts are 37, 49, and 62 mV dec^{-1}, respectively. These results indicate that the $(FeCoNiMnV)_xO$ catalyst exhibits better OER performance.

EIS was conducted at a constant overpotential of 300 mV to investigate the electrode kinetics during the OER. As shown in Fig. 3(d), the Nyquist plots in the high-frequency range exhibit standard semicircles, the diameters of which are determined by the charge-transfer resistance (R_{ct}). The $(FeCoNiMnV)_xO$ catalyst demonstrates an R_{ct} of approximately 5.99 Ω, significantly smaller than the $(FeCoNiMnV)_xO$-200 (approximately 10.47 Ω) and $(FeCoNiMnV)_xO$-240 (approximately 45.30 Ω) catalysts. This observation indicates a rapid charge-transfer rate in the $(FeCoNiMnV)_xO$ catalyst [42–44]. Furthermore, the intersection of the curve with the abscissa indicates that R_s is approximately 2.00 Ω, which can be used for the iR correction. Electrochemical stability is a critical aspect for assessing the catalyst performance during the OER. A long-term stability test was conducted for 50 h at a constant current density of 1000 mA cm^{-2} (Fig. 3(f)), revealing no significant increase in voltage, thus indicating the excellent stability of the $(FeCoNiMnV)_xO$ catalyst for the OER.

To gain insight into the intrinsic OER activity, we evaluated the ECSA of the synthesized catalysts, as shown in Fig. 3(e). The $(FeCoNiMnV)_xO$ catalyst exhibits a considerable C_{dl} value of 6.65 mF cm^{-2} compared with the $(FeCoNiMnV)_xO$-200 (1.05 mF cm^{-2}) and $(FeCoNiMnV)_xO$-240 (1.85 mF cm^{-2}) catalysts. The CV curves of the as-prepared catalysts at scan rates of 10, 20, 30, 40, 50, 60, 70, 80, 90, and 100 mV s^{-1} in the non-faradaic region are shown in Figs. 4(b)–(d). The ECSA values were 166.25, 26.25, and 46.25 for the $(FeCoNiMnV)_xO$, $(FeCoNiMnV)_xO$-200, and $(FeCoNiMnV)_xO$-240 catalysts, respectively (Fig. 4(a)). The higher ECSA observed for the $(FeCoNiMnV)_xO$ catalyst indicates a larger exposed active surface area, contributing to the enhancement of the OER performance [39,45].

4. Conclusion

A low-temperature oil-phase method was used to fabricate high-entropy oxide [$(FeCoNiMnV)_xO$] catalysts. The $(FeCoNiMnV)_xO$-220 catalyst exhibits the highest OER activity, attributed to the abundant exposed active sites and high conductivity. The $(FeCoNiMnV)_xO$ catalyst displayed a low overpotential of 264 mV at 10 mA cm^{-2}, small Tafel slope of 37 mV dec^{-1}, and long-term stability of 50 h, comparable to other reported OER catalysts.

Declaration of Competing Interest

The authors declare that they have no competing financial interests or personal relationships that may have influenced the work reported in this study.

Acknowledgements

We appreciate the contribution of Liping Luo.

Supplementary materials

Supplementary material associated with this article can be found, in the online version, at doi:10.1016/j.chphma.2023.08.002.

References

[1] D.H. Park, M.H. Kim, M. Kim, J.H. Byeon, J.S. Jang, J.H. Kim, D.M. Lim, S.H. Park, Y.H. Gu, J. Kim, K.W. Park, Spherical nickel doped cobalt phosphide as an anode catalyst for oxygen evolution reaction in alkaline media: From catalysis to system, Appl. Catal., B. 327 (2023) 122444, doi:10.1016/j.apcatb.2023.122444.

[2] L. Li, P. Wang, Q. Shao, X. Huang, Recent progress in advanced electrocatalyst design for acidic oxygen evolution reaction, Adv. Mater. 33 (2021) e2004243, doi:10.1002/adma.202004243.

[3] T. Li, X. Zhao, M. Getaye Sendeku, X. Zhang, L. Xu, Z. Wang, S. Wang, X. Duan, H. Liu, W. Liu, D. Zhou, H. Xu, Y. Kuang, X. Sun, Phosphate-decorated Ni_3Fe-LDHs@CoP_x nanoarray for near-neutral seawater splitting, Chem. Eng. J. 460 (2023) 141413, doi:10.1016/j.cej.2023.141413.

[4] D. Wang, C. Duan, H. He, Z. Wang, Z. R, H. Sun, Y. Liu, C. Liu, Microwave solvothermal synthesis of component-tunable high-entropy oxides as high-efficient and stable electrocatalysts for oxygen evolution reaction, J. Colloid Interface Sci. 646 (2023) 89–97, doi:10.1016/j.jcis.2023.05.043.

[5] X. Li, Z. Zhang, M. Shen, Z. Wang, R. Zheng, H. Sun, Y. Liu, D. Wang, C. Liu, Highly efficient oxygen evolution reaction enabled by phosphorus-boron facilitating surface reconstruction of amorphous high-entropy materials, J. Colloid Interface Sci. 628 (2022) 242–251, doi:10.1016/j.jallcom.2020.156158.

[6] S. Wang, W. Huo, F. Fang, Z. Xie, J.K. Shang, J. Jiang, High entropy alloy/C nanoparticles derived from polymetallic MOF as promising electrocatalysts for alkaline oxygen evolution reaction, Chem. Eng. J. 429 (2022) 132410, doi:10.1016/j.cej.2021.132410.

[7] J. Li, J. Li, J. Ren, H. Hong, D. Liu, L. Liu, D. Wang, Electric-field-treated Ni/Co_3O_4 film as high-performance bifunctional electrocatalysts for efficient overall water splitting, Nano-Micro. Lett. 14 (2022) 148, doi:10.1007/s40820-022-00889-3.

[8] P. Wang, Y. Luo, G. Zhang, Z. Chen, H. Ranganathan, S. Sun, Z. Shi, Interface engineering of Ni_xS_y@MnO_xH_y nanorods to efficiently enhance overall-water-splitting activity and stability, Nano-Micro. Lett. 14 (2022) 120, doi:10.1007/s40820-022-00860-2.

[9] X. Li, Z. Zhang, M. Shen, Z. Wang, R. Zheng, H. Sun, Y. Liu, D. Wang, C. Liu, Highly efficient oxygen evolution reaction enabled by phosphorus-boron facilitating surface reconstruction of amorphous high-entropy materials, Chem. Commun. 59 (2023) 5098–5101, doi:10.1016/j.jcis.2022.08.068.

[10] M. Hao, J. Chen, J. Chen, K. Wang, J. Wang, F. Lei, P. Hao, X. Sun, J. Xie, B. Tang, Lattice-disordered high-entropy metal hydroxide nanosheets as efficient precatalysts for bifunctional electro-oxidation, J. Colloid Interface Sci. 642 (2023) 41–52, doi:10.1016/j.jcis.2023.03.152.

[11] J. Li, Y. Hu, X. Huang, Y. Zhu, D. Wang, Bimetallic phosphide heterostructure coupled with ultrathin carbon layer boosting overall alkaline water and seawater splitting, Small (2023) 2206533, doi:10.1002/smll.202206533.

[12] C. Kou, J. Zhou, H. Wang, J. Han, M. Han, A. Vomiero, Y. Liu, H. Liang, Boron pretreatment promotes phosphorization of FeNi catalysts for oxygen evolution, Appl. Catal., B. 330 (2023) 122598, doi:10.1016/j.apcatb.2023.122598.

[13] W. Sun, Y. Wang, S. Liu, F. Lei, J. Xie, B. Tang, High-entropy amorphous oxycyanide as an efficient pre-catalyst for the oxygen evolution reaction, Chem. Commun. 58 (2022) 11981–11984, doi:10.1039/D2CC04646F.

[14] J. Li, M. Guo, X. Yang, J. Wang, K. Wang, A. Wang, F. Lei, P. Hao, J. Xie, B. Tang, Dual elemental modulation in cationic and anionic sites of the multi-metal Prussian blue analogue pre-catalysts for promoted oxygen evolution reaction, Prog. Nat. Sci.-Mater. 32 (2022) 705–714, doi:10.1016/j.pnsc.2022.12.001.

[15] L.A. Stern, L. Feng, F. Song, X. Hu, Ni_2P as a Janus catalyst for water splitting: The oxygen evolution activity of Ni_2P nanoparticles, Energy Environ. Sci. 8 (2015) 2347–2351, doi:10.1039/c5ee01155h.

[16] L. Yu, L. Wu, B. McElhenny, S. Song, D. Luo, F. Zhang, Y. Yu, S. Chen, Z. Ren, Ultrafast room-temperature synthesis of porous S-doped Ni/Fe (oxy)hydroxide electrodes for oxygen evolution catalysis in seawater splitting, Energy Environ. Sci. 13 (2020) 3439–3446, doi:10.1039/d0ee00921k.

[17] D. Li, C. Liu, W. Ma, S. Xu, Y. Lu, W. Wei, J. Zhu, D. Jiang, Fe-doped NiCoP/Prussian blue analog hollow nanocubes as an efficient electrocatalyst for oxygen evolution reaction, Electrochim. Acta. 367 (2021) 137492, doi:10.1016/j.electacta.2020.137492.

[18] Y. Qi, Q. Zhang, S. Meng, D. Li, W. Wei, D. Jiang, M. Chen, Iron-doped nickel cobalt ternary phosphide hyperbranched hierarchical arrays for efficient overall water splitting, Electrochim. Acta. 334 (2020) 135633, doi:10.1016/j.electacta.2020.135633.

[19] P. Zhai, Y. Zhang, Y. Wu, J. Gao, B. Zhang, S. Cao, Y. Zhang, Z. Li, L. Sun, J. Hou, Engineering active sites on hierarchical transition bimetal oxides/sulfides heterostructure array enabling robust overall water splitting, Nat. Commun. 11 (2020) 5462, doi:10.1038/s41467-020-19214-w.

[20] S. Yuan, J. Peng, B. Cai, Z. Huang, A.T. Garcia-Esparza, D. Sokaras, Y. Zhang, L. Giordano, K. Akkiraju, Y.G. Zhu, R. Hübner, X. Zou, Y. Román-Leshkov, Y. Shao-Horn, Tunable metal hydroxide-organic frameworks for catalyzing oxygen evolution, Nat. Mater. 21 (2022) 673–680, doi:10.1038/s41563-022-01199-0.

[21] K. Zhang, R. Zou, Advanced transition metal-based OER electrocatalysts: Current status, opportunities, and challenges, Small 17 (2021) 2100129, doi:10.1002/smll.202100129.

[22] J.S. Yoo, X. Rong, Y. Liu, A.M. Kolpak, Role of lattice oxygen participation in understanding trends in the oxygen evolution reaction on perovskites, ACS Catal. 8 (2018) 4628–4636, doi:10.1021/acscatal.8b00612.

[23] S. Sun, Y. Sun, Y. Zhou, S. Xi, X. Ren, B. Huang, H. Liao, L.P. Wang, Y. Du, Z.J. Xu, Shifting oxygen charge towards octahedral metal: A way to promote water oxidation on cobalt spinel oxides, Angew. Chem. Int. Ed. 58 (2019) 6042–6047, doi:10.1002/anie.201902114.

[24] D. Feng, Y. Dong, L. Zhang, X. Ge, W. Zhang, S. Dai, Z.A. Qiao, Holey lamellar high-entropy oxide as an ultra-high-activity heterogeneous catalyst for solvent-free aerobic oxidation of benzyl alcohol, Angew. Chem. Int. Ed. 59 (2020) 19503–19509, doi:10.1002/anie.202004892.

[25] R. Wei, X. Bu, W. Gao, R.A.B. Villaos, G. Macam, Z.Q. Huang, C. Lan, F.C. Chuang, Y. Qu, J.C. Ho, Engineering surface structure of spinel oxides via high-valent vanadium doping for remarkably enhanced electrocatalytic oxygen evolution reaction, ACS Appl. Mater. Interfaces. 11 (2019) 33012–33021, doi:10.1021/acsami.9b10868.

[26] Y. Zhang, T. Lu, Y. Ye, W. Dai, Y. Zhu, Y. Pan, Stabilizing oxygen vacancy in entropy-engineered $CoFe_2O_4$-type catalysts for co-prosperity of efficiency and stability in an oxygen evolution reaction, ACS Appl. Mater. Interfaces. 12 (2020) 32548–32555, doi:10.1021/acsami.0c05916.

[27] A. Sarkar, Q. Wang, A. Schiele, M.R. Chellali, S.S. Bhattacharya, D. Wang, T. Brezesinski, H. Hahn, L. Velasco, B. Breitung, High-entropy oxides: Fundamental aspects and electrochemical properties, Adv. Mater 31 (2019) 1806236, doi:10.1002/adma.201806236.

[28] O. Gharbi, M.T.T. Tran, B. Tribollet, M. Turmine, V. Vivier, Revisiting cyclic voltammetry and electrochemical impedance spectroscopy analysis for capacitance measurements, Electrochim. Acta. 343 (2020) 136109, doi:10.1016/j.electacta.2020.136109.

[29] M. Han, N. Wang, B. Zhang, Y. Xia, J. Li, J. Han, K. Yao, C. Gao, C. He, Y. Liu, Z. Wang, A. Seifitokaldani, X. Sun, H. Liang, High-valent nickel promoted by atomically embedded copper for efficient water oxidation, ACS Catal. 10 (2020) 9725–9734, doi:10.1021/acscatal.0c01733.

[30] L. Wu, L. Yu, Q. Zhu, B. McElhenny, F. Zhang, C. Wu, X. Xing, J. Bao, S. Chen, Z. Ren, Boron-modified cobalt iron layered double hydroxides for high-efficiency seawater oxidation, Nano Energy 83 (2021) 105838, doi:10.1016/j.nanoen.2021.105838.

[31] H. Yang, Y. Liu, S. Luo, Z. Zhao, X. Wang, Y. Luo, Z. Wang, J. Jin, J. Ma, Lateral-size-mediated efficient oxygen evolution reaction: Insights into the atomically thin quantum dot structure of $NiFe_2O_4$, ACS Catal. 7 (2017) 5557–5567, doi:10.1021/acscatal.7b00007.

[32] A. Ahlawat, V.G. Sathe, Raman study of $NiFe_2O_4$ nanoparticles, bulk and films: Effect of laser power, J. Raman Spectrosc. 42 (2011) 1087–1094, doi:10.1002/jrs.2791.

[33] L. Wu, L. Yu, B. McElhenny, X. Xing, D. Luo, F. Zhang, J. Bao, S. Chen, Z. Ren, Rational design of core-shell-structured CoP_x@FeOOH for efficient seawater electrolysis, Appl. Catal., B. 294 (2021) 120256, doi:10.1016/j.apcatb.2021.120256.

[34] C. Liang, P. Zou, A. Nairan, Y. Zhang, J. Liu, K. Liu, S. Hu, F. Kang, H.J. Fan, C. Yang, Exceptional performance of hierarchical Ni-Fe oxyhydroxide@NiFe alloy nanowire array electrocatalysts for large current density water splitting, Energy Environ. Sci. 13 (2020) 86–95, doi:10.1039/c9ee02388g.

[35] Z. Zheng, D. Wu, G. Chen, N. Zhang, H. Wan, X. Liu, R. Ma, Microcrystallization and lattice contraction of NiFe LDHs for enhancing water electrocatalytic oxidation, Carbon Energy 4 (2022) 901–913, doi:10.1002/cey2.215.

[36] L. Zhang, W. Cai, N. Bao, Top-level design strategy to construct an advanced high-entropy Co-Cu-Fe-Mo (Oxy)hydroxide electrocatalyst for the oxygen evolution reaction, Adv. Mater. 33 (2021) 2100745, doi:10.1002/adma.202100745.

[37] Y. Zhang, H. Guo, P. Yuan, K. Pang, B. Cao, X. Wu, L. Zheng, R. Song, Structural evolution of $CoMoO_4$ to CoOOH by ion electrochemical etching for boosting oxygen evolution reaction, J. Power Sources. 442 (2019) 227252, doi:10.1016/j.jpowsour.2019.227252.

[38] J. Han, S. Hao, Z. Liu, A.M. Asiri, X. Sun, Y. Xu, In situ development of amorphous Mn-Co-P shell on $MnCo_2O_4$ nanowire array for superior oxygen evolution electrocatalysis in alkaline media, Chem. Commun. 54 (2018) 1077–1080, doi:10.1039/c7cc08895g.

[39] B. Talluri, K. Yoo, J. Kim, High entropy spinel metal oxide $(CoCrFeMnNi)_3O_4$ nanoparticles as novel efficient electrocatalyst for methanol oxidation and oxygen evolution reactions, J. Environ. Chem. Eng. 10 (2022) 106932, doi:10.1016/j.jece.2021.106932.

[40] Z. Li, J. Yang, Z. Chen, C. Zheng, L.Q. Wei, Y. Yan, H. Hu, M. Wu, Z. Hu, V, Bridged Co-O to eliminate charge transfer barriers and drive lattice oxygen oxidation during water-splitting, Adv. Funct. Mater. 31 (2020) 2008822, doi:10.1002/adfm.202008822.

[41] J. Jiang, F. Sun, S. Zhou, W. Hu, H. Zhang, J. Dong, Z. Jiang, J. Zhao, J. Li, W. Yan, M. Wang, Atomic-level insight into super-efficient electrocatalytic oxygen evolution on iron and vanadium Co-doped nickel (oxy)hydroxide, Nat. Commun. 9 (2018) 2885, doi:10.1038/s41467-018-05341-y.

[42] Y. Chen, H. Yao, F. Kong, H. Tian, G. Meng, S. Wang, X. Mao, X. Cui, X. Hou, J. Shi, V_2C MXene synergistically coupling FeNi LDH nanosheets for boosting oxygen evolution reaction, Appl. Catal., B. 297 (2021) 120474, doi:10.1016/j.apcatb.2021.120474.

[43] J. Chen, Q. Long, K. Xiao, T. Ouyang, N. Li, S. Ye, Z.Q. Liu, Vertically-interlaced NiFeP/MXene electrocatalyst with a tunable electronic structure for high-efficiency oxygen evolution reaction, Sci. Bull. 66 (2021) 1063–1072, doi:10.1016/j.scib.2021.02.033.

[44] N. Li, J. Han, K. Yao, M. Han, Z. Wang, Y. Liu, L. Liu, H. Liang, Synergistic phosphorized NiFeCo and MXene interaction inspired the formation of high-valence metal sites for efficient oxygen evolution, J. Mater. Sci. Technol. 106 (2022) 90–97, doi:10.1016/j.jmst.2021.08.007.

[45] X. Zhang, H. Yi, M. Jin, Q. Lian, Y. Huang, Z. Ai, R. Huang, Z. Zuo, C. Tang, A. Amini, F. Jia, S. Song, C. Cheng, In situ reconstructed Zn doped $Fe_xNi_{(1-x)}OOH$ catalyst for efficient and ultrastable oxygen evolution reaction at high current densities, Small 18 (2022) 2203710, doi:10.1002/smll.202203710.